LA-UR-20-23014

Title: A simple hydride model for cerium ejecta particles

Author(s):
Regele, Jonathan David
Harrison, Alan Kent
Schwarzkopf, John Dennis
Buttler, William Tillman

Intended for: Report

Issued: 2020-04-20

A SIMPLE HYDRIDE MODEL FOR CERIUM EJECTA PARTICLES

JONATHAN D. REGELE, ALAN K. HARRISON, JOHN D. SCHWARZKOPF, WILLIAM T. BUTTLER

Cerium ejecta particles form after a shock wave impacts a cerium plate with a known roughness or prescribed surface perturbation. When these particles are ejected into hydrogen or deuterium gas the material reacts exothermically and raises the temperature of the particle relative to the gas. A simple model is developed, assuming that the particle remains intact and spherical, to capture the heat and mass transfer that occurs during this process. Model performance is evaluated by comparing with cerium ejecta experiments where the particles are ejected into deuterium gas at initial pressures of 4 and 8 atm. Overall, the model is able to capture the approximately 400 K increase in particle temperature above the surrounding gas temperature.

Introduction

Ejecta form from Richtmyer-Meshkov (RM) [1, 2] unstable growth of surface perturbations after being impacted by a shock wave. Analytic models exist [3, 4] to describe the evolution of spikes and bubbles that originate from linear surface perturbations (2D unstable sheets) or from single dots (3D spikes). These spikes eventually fragment [5, 6, 7, 8, 9] into individual particles that travel at reasonably well known velocities [4, 10, 11, 12, 13, 14]. The amount of ejecta created is a function of the surface perturbation amplitude and whether the surface is liquid or solid after shock release [15].

The ejecta size/mass and velocity distributions have been studied in both gases and vacuum [16, 17, 18, 19, 20, 21, 22, 23, 24, 25, 26, 27, 28]. It's known [29] that droplets with sufficiently small Ohnesourge numbers and Weber numbers below a critical value of 11 the droplets are relatively stable and do not breakup much further. In more recent studies [30, 31] of shocked cerium and tin in vacuum, helium and deuterium gases, cerium ejecta particles react with deuterium gas to form cerium dihydride. The exothermic reaction raises the temperature of the particles relative to the gas temperature by up to 400-500 K. In these experiments [30, 31] the tin particles are liquid with an observed mean diameter of 2 μm while the cerium particles are solid with a mean diameter of 13μm.

A wide range of particle combustion models exist and are summarized in [32, 33, 34] among others. High ash content coal combustion models assume that a layer of ash grows around the outer surface of a reacting coal particle as the char-ash interface moves closer to the particle center. The reaction proceeds as a non-volatile heterogeneous surface reaction. Schwarzkopf *et al.* [35] developed a model for cerium hydriding in deuterium gas that is very similar to the 1-D high ash content model described in [34] where the chemical reaction is controlled by the rate of diffusion through the outer hydride layer.

In this work a similar model is developed that accounts for the spherical nature of the particle along with some other minor differences in model parameters. In section 1, assumptions are made about how to describe the particle and a model is developed for heat and mass transfer. Verification and validation are performed in section 2 to demonstrate the overall accuracy of the model. Section 3 contains details about the numerical integration technique used and the model performance under a variety of conditions is illustrated in section 4 . Conclusions are made in section 5.

1. Mathematical Model

The evolution of cerium ejecta particles is a function of a number of different physical processes, including chemical reactions, heat and mass transfer. In order to develop a simple model of the hydriding process of cerium particles in a deuterium gas, a number of assumptions must be made to simplify the physics involved for the particle:

- the ejecta particles are hydrodynamically stable and spherical
- deuterium must diffuse through a solid layer of cerium dihydride before reaching the unreacted cerium
- deuterium diffuses through the dihydride layer in a quasi-steady manner such that the reaction at the pure cerium surface occurs rapidly
- heat conducts much faster inside the particle relative to the surrounding gas so that the particle temperature can be assumed to be constant.

These assumptions lead to the model illustrated in Fig. 1 where cerium is located in the center of the particle with radius a and a solid dihydride layer surrounds that region with radius b. Deuterium must diffuse through the dihydride layer until it reacts rapidly with the cerium. As the cerium reacts, the volume of cerium radius a retreats as the dihydride layer advances. The particle is at a constant temperature T_p and the surrounding gas has a concentration C_∞ or mass fraction Y_∞ and temperature T_∞.

1.1. **Molecular diffusion.** It is assumed that the particles are spherical, hydrodynamically stable and do not breakup any further. The deuterium gas diffuses through a solid layer of cerium dihydride where the gas concentration far away from the particle is C_∞ or the mass fraction is Y_∞. The time unsteady molecular diffusion concentration equation describing this process is expressed

$$\frac{\partial C}{\partial t} = \boldsymbol{\nabla} \cdot \mathcal{D} \boldsymbol{\nabla} C \tag{1}$$

or in terms of mass fraction as

$$\frac{\partial Y}{\partial t} = \boldsymbol{\nabla} \cdot \mathcal{D} \boldsymbol{\nabla} Y \tag{2}$$

where C is the concentration of deuterium anywhere inside the particle, D is the diffusion coefficient of deuterium through a solid layer of cerium dihydride, and Y is the mass fraction. If the particle is hydrodynamically stable, it can be assumed that the particles are at least close to spherical in nature and the laplacian is limited to the radial direction.

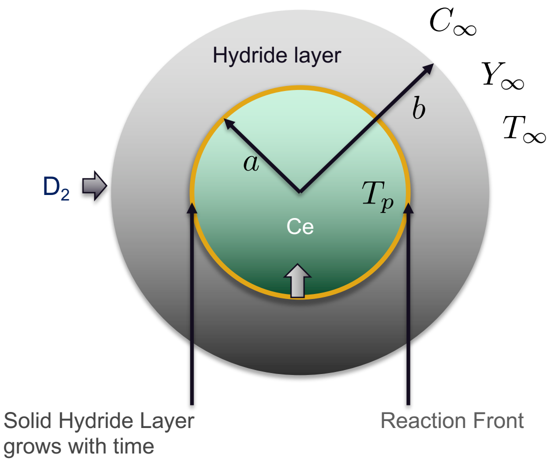

FIGURE 1. Diagram of an ejecta particle with pure cerium surrounded by a layer of cerium dihydride.

Additionally, if the diffusion coefficient is assumed to be constant the above equation becomes

$$\frac{\partial Y}{\partial t} = \mathcal{D}\left(\frac{\partial^2 Y}{\partial r^2} + \frac{2}{r}\frac{\partial Y}{\partial r}\right). \tag{3}$$

Finally, it can be reasonably assumed that the reaction at the cerium surface occurs fast enough that the reaction is diffusion controlled and the concentration of deuterium at the cerium/cerium dihydride interface is negligible ($Y_s = 0$). This is a common assumption in particle combustion models [32, 33, 34] and will be employed here. The resulting differential equation becomes

$$\mathcal{D}\frac{d}{dr}\left(r^2\frac{dY}{dr}\right) = 0\,. \tag{4}$$

The solution for the mass fraction as a function of radius is

$$Y(r) = Y_\infty \frac{ab}{a-b}\left(\frac{1}{r} - \frac{1}{a}\right). \tag{5}$$

The mass flux of deuterium reaching the pure cerium surface is evaluated

$$G_{D_2} = -\rho_{D_2}\mathcal{D}\left.\frac{dY}{dr}\right|_{r=a} = \mathcal{D}\frac{\rho_\infty Y_\infty}{b-a}\frac{b}{a}\,. \tag{6}$$

Here ρ_{D_2} is the density of the gas inside the hydride layer, ρ_∞ is the ambient gas density, Y_∞ is the ambient gas mass fraction, b is the particle outer radius and a is the radius of the cerium/cerium dihydride interface. It's clear that the mass flux $G \to \infty$ when $b = a$ or $a \to 0$. When $b = a$ the hydride layer has zero thickness, which suggests that the rate

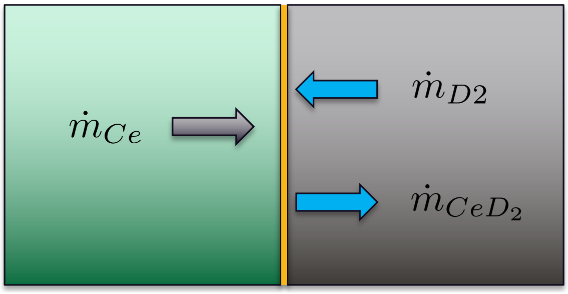

FIGURE 2. Diagram illustrating the movement of cerium, deuterium and cerium dihydride relative to the reaction interface highlighted in yellow. Pure cerium is on the left in green and deuterium diffuses through the solid cerium dihydride before reaching the reaction interface.

limiting step at that point in time would be the chemical kinetics on the initially unreacted cerium surface.

1.2. **Reaction model.** Cerium reacts with deuterium to form CeD_2 after which it can continue to produce CeD_3. The second reaction is slower than the first and doesn't always run to completion so that the final reaction product becomes CeD_{2+x}, where $x \in [0, 1]$ [36]. The details of determining the final product composition is beyond the scope of the present work, thus only the first reaction is considered at this time. The reaction can then be written

$$\mathrm{Ce} + \mathrm{D}_2 \rightarrow \mathrm{CeD}_2\,, \tag{7}$$

where one deuterium molecule reacts with each cerium atom. In this instance, the mass stoichiometric coefficient for this reaction is written as a ratio of molecular weights

$$i = \frac{W_{Ce}}{W_{D_2}}\,, \tag{8}$$

which can also be related to the ratio of mass flows and mass fluxes

$$i = \frac{\dot{m}_{Ce}}{\dot{m}_{D_2}} = \frac{G_{Ce}}{G_{D_2}}\,, \tag{9}$$

where the mass flux G is the mass flow rate per unit area at the cerium/hydride interface. The mass stoichiometric coefficient can be used to rewrite Eq. 7 in terms of mass so that

$$(i\,\mathrm{kg})\,\mathrm{Ce} + (1\,\mathrm{kg})\,\mathrm{D}_2 \rightarrow (i+1\,\mathrm{kg})\,\mathrm{CeD}_2\,. \tag{10}$$

Now the mass consumption rate of cerium can be directly related to the mass consumption rate of deuterium so that

$$\dot{m}_{Ce} = i\dot{m}_{D_2}\,. \tag{11}$$

Figure **??** illustrates the flow of the reactant and product species relative to the reaction front highlighted in yellow. Deuterium diffuses through the solid cerium dihydride layer and reacts instantly upon reaching the cerium surface. Mass conservation relative to the reaction front is written

$$\dot{m}_{CeD_2} = \dot{m}_{Ce} + \dot{m}_{D_2} \tag{12}$$

or in terms of mass flux at the reaction surface

$$G_{CeD_2} = G_{Ce} + G_{D_2}\,. \tag{13}$$

Cerium dihydride is less dense than pure cerium, which will cause the particle to grow in size as the particle reacts. While this is not difficult to account for in practice, at this point the densities in both regions will be assumed to be constant so that the outer radius of the particle remains constant. In this case, only the inner radius a changes with time. The mass of cerium inside a sphere is written

$$m_{Ce} = \rho_{Ce}\frac{4}{3}\pi a^3\,. \tag{14}$$

After differentiation with respect to time, the rate of change of cerium mass becomes

$$\dot{m}_{Ce} = \rho_{Ce} 4\pi a^2 \frac{da}{dt} \tag{15}$$

and the mass flux at the liquid surface can be evaluated by to be

$$G_{Ce} = \frac{\dot{m}_{Ce}}{4\pi a^2} = \rho_{Ce}\frac{da}{dt}\,. \tag{16}$$

The mass stoichiometric coefficient is used to find the deuterium mass flux

$$G_{D_2} = \frac{\rho_{Ce}}{i}\frac{da}{dt}\,. \tag{17}$$

The mass flux in Eq. 6 determines the rate at which deuterium diffuses through the cerium dihydride layer and Eq. 17 describes the rate of change of the cerium radius for a given mass flux G_{D_2}. After equating Eq. 6 and Eq. 17 an ODE describing the rate of change of the cerium radius a is obtained

$$\frac{da}{dt} = i\frac{\rho_\infty}{\rho_{Ce}}\frac{Y_\infty \mathcal{D}}{b-a}\frac{b}{a}\,. \tag{18}$$

The inner radius changes rapidly when a is initially equal to b and when $a \to 0$. One-dimensional Cartesian models do not have the b/a term on the right and thereby do not capture the reaction speedup that occurs for small values of a. Otherwise, 1-D models are nearly identical to this model for most of the particle reaction period. This equation can be integrated into a parametric expression for $t = t(a)$ or solved numerically. It should be noted that per MD simulations performed by Daniel Sheppard the diffusivity coefficient increases with temperature.

1.3. **Heat transfer model.** It is common in many particle combustion models [32, 34] to use the lumped capacitance model, which assumes that thermal conduction inside the particle is much faster than convection into the gas so that the particle temperature can be assumed to be uniform. Radiation is assumed to be small relative to convection since the difference in temperature between the two phases is assumed to be small. Convective heat transfer at the surface of the particle and gas is expressed

$$\dot{Q}_c = Nu \pi k_c 2b (T_\infty - T_p)\,, \tag{19}$$

where $\dot{Q}_c$ is the heat transfer rate, Nu is the Nusselt number, k_c is the thermal conductivity of the continuous phase (gas), b is the outer radius, T_∞ is the ambient gas temperature and T_p is the particle temperature. The Ranz-Marshall correlation [37] is a common model for forced convection over spherical particles [38] for Reynolds numbers up to 5 x 10^4 and is written

$$Nu = 2 + 0.6 Re_r^{1/2} Pr^{1/3}\,, \tag{20}$$

where Re_r is the particle Reynolds number using the velocity of the particle relative to the gas and Pr is the Prandtl number.

1.4. **Energy Conservation.** Energy conservation for a reacting particle with heat transfer can be expressed

$$\dot{E}_p = \dot{Q}_r + \dot{Q}_c\,, \tag{21}$$

where $\dot{E}_p$ is the rate of change of internal energy associated with the particle mass, $\dot{Q}_r$ is the heat release from reaction, and $\dot{Q}_c$ is the heat transferred to the particle from the gas given in Eq. 19.

The heat release from reaction can be expressed

$$\dot{Q}_r = \dot{m}_{Ce} h_r\,, \tag{22}$$

where h_r is the heat of reaction or the amount of energy per unit mass of cerium released during a chemical reaction. The heat of reaction is expressed as the difference of product and reactant enthalpies, i.e.

$$h_r = h_{prod} - h_{reac}\,, \tag{23}$$

where according to Eq. 7 h_{prod} is cerium dihydride's enthalpy of formation h_f^0 and $h_{reac} = 0$ for both pure cerium and deuterium at STP.

The energy rate of change inside the particle can be written

$$\dot{E}_p = m_p c^m \frac{dT_p}{dt}\,, \tag{24}$$

where c^m is the specific heat, dT_p/dt is the particle temperature rate of change, and the particle mass is the sum of all masses inside the particle $m_p = m_{Ce} + m_{CeD_2} + m_{D_2}$. Summation of the different terms in Eq. 21 yields

$$\frac{dT_p}{dt} = \frac{Nu}{2}\frac{1}{\tau_T}(t_\infty - T_p) + \frac{\dot{m}_{Ce} h_r}{m_p c^m}\,, \tag{25}$$

where the thermal response time [38] is defined

$$\tau_T = \frac{\rho_p c_p (2b)^2}{12 k_c}\,, \tag{26}$$

where ρ_p is the mean particle density m_p/V_p, c_p is the mean particle specific heat and k_c is the thermal conductivity of the continuous phase (gas).

1.5. **Model summary.** To summarize, the particle hydride model is described with mass and energy conservation equations where mass conservation is expressed as an ordinary differential equation for the cerium particle radius (Eq. 18)

$$\frac{da}{dt} = i\frac{\rho_\infty}{\rho_{Ce}}\frac{Y_\infty \mathcal{D}}{b-a}\frac{b}{a} \tag{27}$$

and energy conservation is written in terms of the particle temperature (Eq. 25)

$$\frac{dT_p}{dt} = \frac{Nu}{2}\frac{1}{\tau_T}(T_\infty - T_p) + \frac{\dot{m}_{Ce} h_r}{m_p c^m}\,. \tag{28}$$

The cerium mass consumption rate is found by combining Eq. 6 and 9 with $\dot{m}_{Ce} = 4\pi a^2 G_{Ce}$ to obtain

$$\dot{m}_{Ce} = i 4\pi a b \mathcal{D}\frac{\rho_\infty Y_\infty}{b-a}\,. \tag{29}$$

It is assumed that an appropriate momentum conservation equation will be solved simultaneously with these two conservation laws.

2. Verification and Validation

The proposed model was coded into python to verify that the model behaves as anticipated and to perform some initial comparisons with experimental data. The model assumes the velocity remains constant and does not change, which limits the applicability of the results to the initial moments after ejecta particles are first created. The analysis also focuses on a single particle, which implies that the multiphase mixture it represents is dilute.

A variety of limiting cases were considered to ensure the equations were coded correctly. The first includes verifying that non-reacting particle temperatures asymptote to the surrounding gas temperature on a timescale on the order of the thermal relaxation time τ_T. This ensures that the heat transfer model works correctly independent from any reactions. The second test focuses on the diffusion controlled reaction and ensures that a particle with diffusion controlled reactions reacts completely in a time that can be computed analytically to be

$$\tau_r = \frac{1}{6i}\frac{\rho_{Ce}}{\rho_{D_2}}\frac{b^2}{\mathcal{D} Y_\infty}\,. \tag{30}$$

This solution is obtained by integrating Eq. 27 to obtain $t(a)$ as a cubic polynomial with b constant and then evaluating $t = \tau_r$ with $a = 0$. Note that this time is 1/3 the time obtained assuming a planar diffusion model because the spherical coordinate system causes

Table 1. Individual input parameters used for the 4 and 8 atm cases.

Initial Gas Pressure [atm]	4	8
Shocked gas temperature T_∞ [K]	720	740
Shocked metal temperature T_p [K]	990	990
Shocked gas density ρ_∞ [kg/m^3]	2.3	4.5
Initial particle velocity u_p [mm/μs]	2.39	2.33
Initial gas velocity u_g [mm/μs]	1.91	1.86
Relative velocity u_r [mm/μs]	0.48	0.47
Offset time t_0 [μs]	0.85	0.80

Quantity	Symbol	Value	
Gas specific heat	c_p^g	7.25	J/kg-K
Metal specific heat	c^m	37.7	J/kg-K
Particle diameter	b	13	μm
Particle density	ρ_p	6680	kg/m^3
Gas thermal Conductivity	k_c	0.1382	W/m-K
Gas dynamic viscosity	μ_c	1.72E-5	Pa-s
CeD$_2$ Heat of formation	h_f^0	210E+6	J/kmol
Particle atomic mass	W_p	140	g/mol
Gas atomic mass	W_c	4.0	g/mol
Gas specific heat ratio	γ	1.4	

Table 2. Common model parameters used for both the 4 and 8 atm cases.

a $1/a$ term to appear in Eq. 27, which speeds up the reaction when the particle diameter becomes small.

Preliminary validation tests were performed by modeling the early stages of cerium ejecta experiments where the ejecta particles react with D_2 gas and show a rise in temperature relative the the surrounding gas. Complete details on these experiments and the post-shock conditions calculated using hydrodynamic simulations can be found in [30, 31]. The experiment consists of a high explosive that sends a shock wave through a cerium plate that is machined so that ejecta particles are created with a mean diameter of $13\mu m$. The gas chamber where the particles are ejected into contains deuterium gas at 4 and 8 atm. Table 1 contains the input parameters for each case.

Table 1 also contains the times when the shock emerges from the cerium material into the deuterium gas. This offset time is used to shift the data so that an accurate temporal comparison can be made between the model and experiment. It should be noted that it does take a finite time between when the shock breaks out of the cerium material and hydrodynamically stable ejecta particles are created. This finite time is not currently taken into account for comparisons with the model, since it is unclear what these times are.

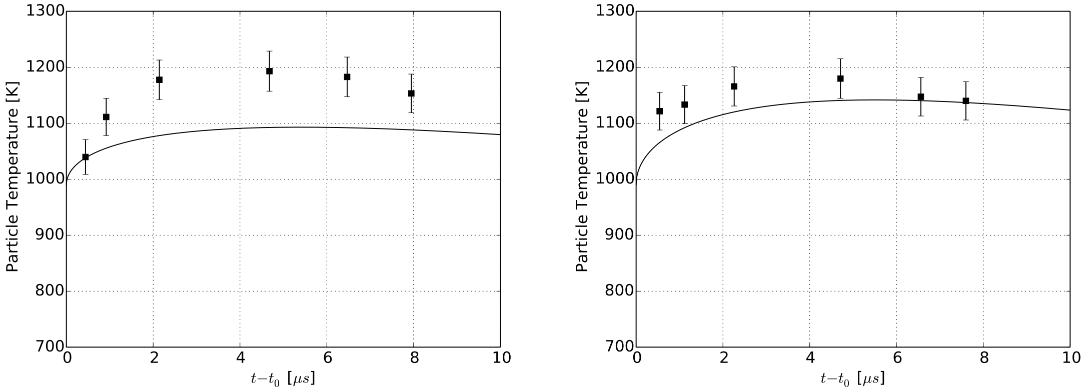

FIGURE 3. Particle temperature as a function of time for 4 (left) and 8 (right) atm cases. The initial gas temperatures are 720 K (left) and 740 K (right).

Table 2 lists the model parameters that are common to both of the 4 and 8 atm cases such as material properties, heat of formation, molecular mass, etc. The diffusivity of D_2 into CeD_2 is calculated using MD simulations for a range of temperatures obtained from Dan Sheppard and an expression for the diffusivity can be expressed as $D(T_p)$ =2.083589E-14 $\cdot T_p^{1.941438}$. Additionally, Sheppard recommends that this diffusivity needs to be multiplied by a factor of 3 to account for the rotational symmetry present. The stoichiometric mass ratio (Eq. 8) is $i = 35$ and the heat of reaction $h_r = h_f^0/W_p =$ 1.5E+6 J/kg. Most of the metal properties were obtained from [39] and the gas properties were obtained from [40]. The heat of formation of cerium dihydride was obtained from Dan Shepard and is consistent with the range of values documented in [36, 41]. Since the particle mass and diameter are assumed to be constant the mass of the particle is simply $m_p = \rho_p \pi b^3/6$ where again $\rho_p = \rho_{Ce}$.

Figure 3 shows the temperature histories for the 4 and 8 atm cases. The experimental time axis is shifted by the offset time t_0 so that $t-t_0 = 0$ corresponds to instantaneous ejecta production after the shock emerges from the cerium material. Although we are assuming instantaneous ejecta production for the moment, in reality it will take a finite amount of time for the Richtmyer-Meshkov spike to destabilize and breakup in to hydrodynamically stable ejecta droplets. If this creation time were included it would shift the experimental data further to the left because the model assumes this state from the beginning.

In both cases, the model (solid line) captures roughly the 400-500 K jump in temperature above the gas temperature (720K for 4atm and 740K for 8atm), but the accuracy varies between the two. In the 4 atm case, the model passes through the first temperature data point, but then is consistently lower than the experimental data for the remaining 5 data points by about 100 K. In the 8 atm case the mean difference between the model and experimental data is less and in general the model comes closer to approximating the experimental data. While the model only passes through the last two data points, the model is only slightly outside the 3% uncertainty range of the second through fourth data points.

It should be noted that at this point only a single particle is considered inside of infinite deuterium gas. In the experiment there is a multiphase mixture of deuterium gas and ejecta particles that transfer momentum, mass and energy in significant quantities between each phase. In order to more accurately estimate the particle temperatures, the temperature rise of the deuterium must be accounted for along with a reduction in the particle relative velocities. However, at this time, the results are compelling enough to believe that with the rough approximations used at this point, these additional corrections will likely lead to more accurate predictions that better capture the transient dynamics of heat release and energy transfer.

3. Numerical Integration Method

The reacting particle evolution equations in Section 1.5 are rewritten here for convenience. The mass conservation equation written in terms of reaction radius is written

$$\frac{da}{dt} = i\frac{\rho_\infty}{\rho_{Ce}}\frac{Y_\infty \mathcal{D}}{b-a}\frac{b}{a} \tag{31}$$

and the internal energy equation for a particle is written

$$\frac{de_p}{dt} = \frac{Nu}{2}\frac{c^m}{\tau_T}(T_\infty - T_p) + \frac{\dot{m}_{Ce} h_r}{m_p}\,. \tag{32}$$

The mass conversion rate required for Eq. 32 is

$$\dot{m}_{Ce} = i4\pi ab\mathcal{D}\frac{\rho_\infty Y_\infty}{b-a}\,. \tag{33}$$

Note that both Eq. 31 and 33 contain roots where real values of $a \in [0, b]$ may lead to division by zero without proper treatment.

Preliminary first order numerical integration schemes of Eq. 31 required $O(10^5)$ timesteps per particle to obtain particle temperatures that were relatively insensitive to timestep size. Upon closer examination, it was determined that Eq. 31 could be integrated analytically. An exact solution remedies both of the potential division by zero scenarios in 31, but there is still the possibility of division by zero in Eq. 33. Section 3.1 presents how the analytical solution is found and the assumptions made to obtain it. Section 3.2 shows how the energy equation is discretized along with the mass conversion rate (Eq. 33).

3.1. **Reaction Radius Integration.** In order to obtain an analytical solution to Eq. 31, it is helpful to simplify the equation into a simple mathematical form. The first step is to transform the reaction radius equation using the reaction time (Eq. 30) and the non-dimensional reaction radius $r = a/b$ so that Eq. 31 becomes

$$\frac{dr}{dt} = \frac{1}{6\tau_r}\frac{1}{1-r}\frac{1}{r}\,. \tag{34}$$

For the moment, it is assumed that every term in Eq. 31 is constant except for the reaction radius a so that τ_r is constant. Under these conditions, Eq. 34 can be integrated to give

$$\frac{t}{\tau_r} = 2r^3 - 3r^2 + 1\,, \tag{35}$$

where $r = 1$ when $t = 0$ and $r = 0$ when $t = \tau_r$. Finally, substitution of $t_* = t/\tau_r$ gives

$$0 = 2r^3 - 3r^2 + (1 - t_*) \tag{36}$$

where $t_* \in [0, 1]$ and $r \in [0, 1]$.

This cubic equation must be solved to obtain the reaction radius r. Visual inspection of the solution for the valid range of t_* shows that the middle root provides the real solution for $0 < t_* < 1$ and double roots when $t_* = 0$ and $t_* = 1$. A trigonometric solution method gives the solution as

$$r(t_*) = \cos\left(\frac{2\pi}{3} - \theta(t_*)\right) + \frac{1}{2} \tag{37}$$

with

$$\theta(t_*) = \frac{1}{3}\arccos(2t_* - 1)\,. \tag{38}$$

This solution assumes that τ_r is constant over the entire reaction period. However, recall that the solution will be used in conjunction with a hydrodynamic fluid solver that integrates in time with a step Δt where τ_r is only assumed to be constant over Δt. The non-dimensional change in radius from timestep n to $n + 1$ with $t_*^{n+1} = t_*^n + \Delta t_*$ can be expressed

$$\Delta r_n^{n+1} = r(t_*^{n+1}) - r(t_*^n) \tag{39}$$

$$= r^{n+1} - r^n \tag{40}$$

$$= \cos\left(\frac{2\pi}{3} - \theta^{n+1}\right) - \cos\left(\frac{2\pi}{3} - \theta^n\right)\,. \tag{41}$$

Transformation back into dimensional variables gives the reaction radius a at $t^n + \Delta t$ as

$$a^{n+1} = a^n + b\Delta r_n^{n+1} \tag{42}$$

with

$$\theta^n = \frac{1}{3}\arccos\left(2\frac{t^n}{\tau_r^n} - 1\right) \qquad \theta^{n+1} = \frac{1}{3}\arccos\left(2\left[\frac{t^n + \Delta t}{\tau_r^n}\right] - 1\right)\,. \tag{43}$$

Equations 42 and 43 provide the reaction radius at $t^{n+1} = t^n + \Delta t$ given the reaction radius a^n at $t = t^n$.

3.2. **Particle Internal Energy Integration.** In order to integrate the energy equation (Eq. 32), the mass conversion rate $\dot{m}_{Ce}$ in Eq. 33 must be a real number for all values of $a \in [0, b]$. The initial reaction radius is $a = b$, which gives an infinite value at the first timestep. In order to resolve this issue, the particle properties are approximated by half-step values (i.e. $t^{n+1/2} = t^n + \Delta t/2$). This approach prevents the potential division by zero possibility while also making the integration scheme implicit.

If the time derivative of the particle's internal energy e_p is discretized with a first order explicit Euler approach the discretized energy equation becomes

$$\frac{\Delta e_p}{\Delta t} = \frac{Nu^n}{2}\frac{c^m}{\tau_T^n}(T_\infty^n - T_p^{n+1/2}) + \frac{\dot{m}_{Ce}^{n+1/2} h_r}{m_p}\,, \tag{44}$$

where the Nusselt number Nu, thermal relaxation time τ_T and the gas temperature T_∞^n are evaluated at t^n. The mean particle temperature is

$$T^{n+1/2} = \frac{T_p^n + T_p^{n+1}}{2} \tag{45}$$

and the mean particle internal energy is related to the mean particle temperature by the particle specific heat so that $e^{n+1/2} = c^m T_p^{n+1/2} = e^n + \Delta e_p/2$. Combining these gives

$$\frac{\Delta e_p}{\Delta t}\left(1 + \frac{\Delta t}{\tau_T^n}\frac{Nu^n}{4}\right) = \frac{Nu^n}{2}\frac{c^m}{\tau_T^n}(T_\infty - T_p^n) + \frac{\dot{m}_{Ce}^{n+1/2} h_r}{m_p}\,, \tag{46}$$

where the change in internal energy for a particle Δe_p can be evaluated and used to update the internal energy at $e_p^{n+1} = e_p^n + \Delta e_p$.

The average mass conversion rate $\dot{m}_{Ce}^{n+1/2}$ is evaluated using Eq. 33

$$\dot{m}_{Ce}^{n+1/2} = i4\pi a^{n+1/2} b\mathcal{D}\frac{\rho_\infty Y_\infty}{b - a^{n+1/2}}\,, \tag{47}$$

where $a^{n+1/2} = a^n + b\Delta r_n^{n+1/2}$ and Eq. 41 can be evaluated at a half step to obtain

$$\Delta r_n^{n+1/2} = \cos\left(\frac{2\pi}{3} - \theta^{n+1/2}\right) - \cos\left(\frac{2\pi}{3} - \theta^n\right) \tag{48}$$

with

$$\theta^{n+1/2} = \frac{1}{3}\arccos\left(2\left[\frac{t^n + \Delta t/2}{\tau_r^n}\right] - 1\right)\,. \tag{49}$$

Again, the possibility to divide by zero when $a = b$ is avoided by using the mass conversion rate $\dot{m}_{Ce}$ at a half-step.

Note that the process of obtaining the mass conversion rate at $t^{n+1/2}$ requires the reaction radius to be computed at that time as well. Thus, two timesteps are performed for the reaction radius during each interval Δt. The final reaction radius is obtained using $a^{n+1} = a^{n+1/2} + b\Delta r_{n+1/2}^{n+1}$, where

$$\Delta r_{n+1/2}^{n+1} = \cos\left(\frac{2\pi}{3} - \theta^{n+1}\right) - \cos\left(\frac{2\pi}{3} - \theta^{n+1/2}\right)\,, \tag{50}$$

$\theta^{n+1/2}$ is given in Eq. 49 and

$$\theta^{n+1} = \frac{1}{3}\arccos\left(2\left[\frac{t^{n+1/2}+\Delta t/2}{\tau_r^n}\right]-1\right) . \tag{51}$$

3.3. Code Implementation.

The numerical integration scheme presented in the preceeding sections is implemented into the code as a `diffcontrol` class underneath the parent class `hydride` that was created to contain the current and any future reaction models. The entire path to the diffcontrol model is
`/global/mesh/mat/gas/model/ejecta/transformation/hydride/diffcontrol`
where the material `mat` is from the source material. At the moment, many of the model parameters are set from within the `diffcointrol` class. These include

- `stoich_mass_ratio`: stoichiometric mass ratio i
- `diffusion_coefficient`: gas diffusion rate through hydride layer $\mathcal{D}$
- `thermal_conductivity`: gas thermal conductivity k_c
- `heat_of_reaction`: energy release per unit mass of reactant h_r
- `spec_heat_ptcl`: specific heat of particle c^m
- `gamma`: gas phases specific heat ratio γ
- `p_mu`: constant viscosity of the gas μ_c
- `pr`: gas phase Prandtl number Pr .

There are a total of 8 parameters, but the 5 highlighted blue can likely be derived from other material properties and classes in the code. Later revisions will attempt to derive these properties from other nodes when ejecta are first created.

Even though an analytical solution is used for the reaction radius, it is still possible for the reaction radius to become negative. Thus, after each iteration the reaction radius is limited by the maximum of its value and zero, i.e. $a = \max(a, 0)$. Additionally, once the reaction radius is equal to zero it is not necessary to perform the reaction radius integration outlined in section 3. Thus, the reaction step is only performed when $a > 0$.

4. Model Performance

The implemented model equations were verified to be correct by reproducing exactly the fully converged model particle temperatures of the 4 atm and 8 atm cases generated from the Python code in Fig. 3. Additionally, limiting cases were performed to verify that the particle temperatures asymptote to the correct steady-state temperature for a constant mass conversion rate $\dot{m}_{Ce}$.

It was noted at the beginning of Sec. 3 that an implicit first order time integration scheme was initially tested in the code. Figure 4 compares the particle temperatures from the exact and implicit first order schemes for three decades of timestep sizes. The experimental data from the experiments is included for reference. As noted earlier, the converged model temperature is lower than the experimental temperatures, but the first order implicit time integration solution is consistently higher than the converged solution and the deviation increases as the timestep is increased. However, there is no visible difference in accuracy for the solution method that uses an exact solution to the reaction radius equation.

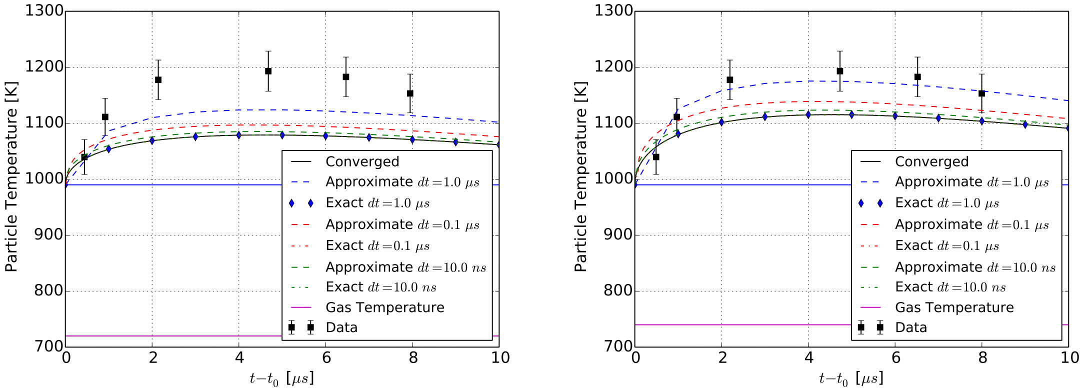

FIGURE 4. Comparison of particle temperatures produce by first order implicit and exact reaction equation solutions for 4 (left) and 8 (right) atm cases. Horizontal magenta lines indicate initial gas temperatures are 720 K (left) and 740 K (right) and horizontal blue lines indicate initial particle temperatures (990 K).

The temperature curves shown in Fig. 4 are for particles with a 13μm diameter. In order to evaluate the accuracy and stability of the model for smaller particles, the 8 atm case was performed with particle sizes of 1.3μm and 0.13μm. The temperature histories for these cases are shown in Fig. 5. The timestep sizes analyzed range from 0.1μs to 0.001μs for the 1.3μm diameter particles and 3 ns to 0.03 ns for the 0.13μm diameter particles. With the exception of the largest timesteps the solution is converged. As a rule of thumb, converged particle temperatures can be obtained by using timesteps $dt < \tau_r/100$, which is significantly better than the $O(10^5)$ timesteps required for the first order implicit method.

The initial assumption used to initially develop the model assumed that the velocity remains relatively constant during the course of the measured reaction period. Once the model is implemented into our multiphase flow solver, it is possible to include other transport effects such as momentum coupling. Figure 6 compares particle temperatures for the 4 and 8 atm cases with no momentum coupling and with one-way coupling (particles slow down, but do not accelerate the gas). The initial temperature rise is identical, but after 2-3μs the temperatures with momentum coupling rise slightly faster than the uncoupled particles. This occurs because as the particle speed is reduced from drag the heat transfer rate from the particle to the gas is reduced and the particle temperature is increased. Overall, the difference in temperature between the two is relatively minor, which verifies the validity of the initial constant velocity assumption for model development purposes.

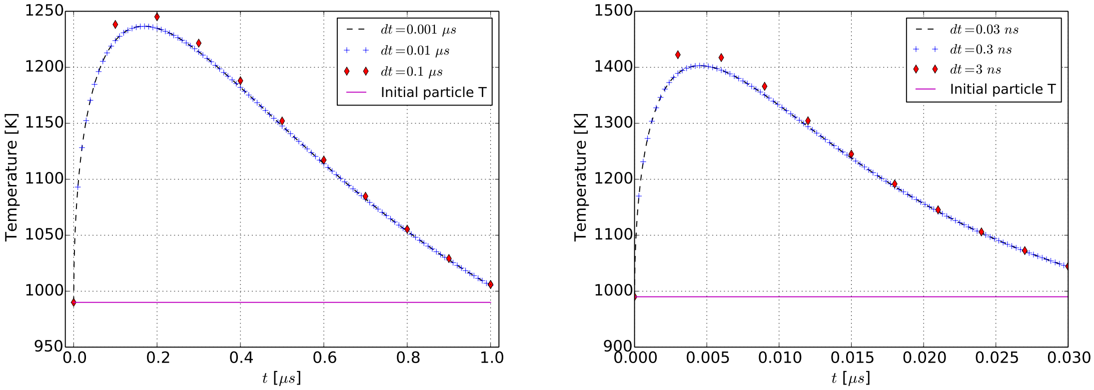

FIGURE 5. Particle temperatures with different timestep sizes for particle diameters equal to 1.3μm (left) and 0.13μm (right), respectively. Properties other than the particle diameters are identical to the 8 atm case.

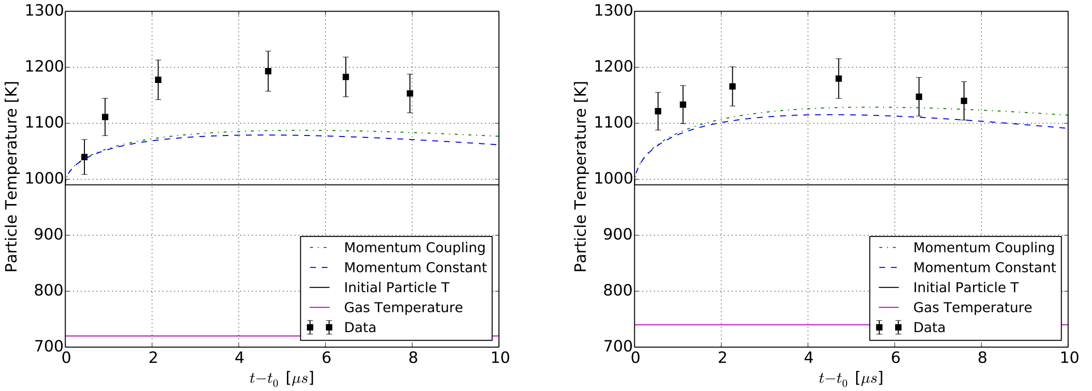

FIGURE 6. Particle temperatures with and without momentum coupling for the 4 atm (left) 8 atm (right) cases, respectively.

5. CONCLUSIONS

A simple model is developed to capture the exothermic hydride reaction of cerium material ejected into a deuterium gas. The model assumes the particle remains spherical, is hydrodynamically stable and does not breakup beyond its initial size. The hydride reaction is controlled by diffusion of deuterium through the hydride layer and reacts infinitely fast at the pure cerium metal surface. Despite the simplicity of the model conditions relative to the experiment, the model is able to roughly estimate the 400 K increase in particle temperature above the surrounding gas temperature. It is likely that the transient details will be better represented when additional details are accounted for such finite disperse phase volume fraction, gas phase temperature increase and hydride layer volume expansion.

References

[1] Robert D. Richtmyer. Taylor instability in shock acceleration of compressible fluids. *Communications on Pure and Applied Mathematics*, 13(2):297–319, 1960.

[2] E. E. Meshkov. Instability of the interface of two gases accelerated by a shock wave. *Fluid Dynamics*, 4(5):101–104, 1969.

[3] David Layzer. On The Instability Of Superposed Fluids in a Gravitational Field. *Astrophysical Journal*, 122(1):1–12, 1955.

[4] Karnig O. Mikaelian. Analytic approach to nonlinear rayleigh-taylor and richtmyer-meshkov instabilities. *Physical Review Letters*, 80(3):508–511, 1998.

[5] O. Durand and L. Soulard. Large-scale molecular dynamics study of jet breakup and ejecta production from shock-loaded copper with a hybrid method. *Journal of Applied Physics*, 111(4), 2012.

[6] O. Durand and L. Soulard. Power law and exponential ejecta size distributions from the dynamic fragmentation of shock-loaded Cu and Sn metals under melt conditions. *Journal of Applied Physics*, 114(19), 2013.

[7] Guy Dimonte, Guillermo Terrones, F. J. Cherne, and P. Ramaprabhu. Ejecta source model based on the nonlinear Richtmyer-Meshkov instability. *Journal of Applied Physics*, 113(2), 2013.

[8] F. J. Cherne, J. E. Hammerberg, M. J. Andrews, V. Karkhanis, and P. Ramaprabhu. On shock driven jetting of liquid from non-sinusoidal surfaces into a vacuum. *Journal of Applied Physics*, 118(18):185901, 2015.

[9] O. Durand and L. Soulard. Mass-velocity and size-velocity distributions of ejecta cloud from shock-loaded tin surface using atomistic simulations. *Journal of Applied Physics*, 117(16), 2015.

[10] Qiang Zhang. Analytical solutions of layzer-type approach to unstable interfacial fluid mixing. *Physical Review Letters*, 81(16):3391–3394, 1998.

[11] Karnig O. Mikaelian. Limitations and failures of the Layzer model for hydrodynamic instabilities. *Physical Review E - Statistical, Nonlinear, and Soft Matter Physics*, 78(1):1–4, 2008.

[12] Karnig O. Mikaelian. Analytic approach to nonlinear hydrodynamic instabilities driven by time-dependent accelerations. *Physical Review E - Statistical, Nonlinear, and Soft Matter Physics*, 81(1):1–16, 2010.

[13] W. T. Buttler, D. M. Oró, D. L. Preston, Karnig O. Mikaelian, F. J. Cherne, R. S. Hixson, F. G. Mariam, C. Morris, J. B. Stone, G. Terrones, and D. Tupa. Unstable Richtmyer–Meshkov growth of solid and liquid metals in vacuum. *J. Fluid Mech.*, 703:60–84, 2012.

[14] V Karkhanis, P Ramaprabhu, F J Cherne, J E Hammerberg, and M J Andrews. A numerical study of bubble and spike velocities in shock-driven liquid metals. *Journal of Applied Physics*, 025902:0–15, 2018.

[15] M. B. Zellner, W. Vogan McNeil, G. T. Gray, D. C. Huerta, N. S.P. King, G. E. Neal, S. J. Valentine, J. R. Payton, J. Rubin, G. D. Stevens, W. D. Turley, and W. T. Buttler. Surface preparation methods to enhance dynamic surface property measurements of shocked metal surfaces. *Journal of Applied Physics*, 103(8), 2008.

[16] J. R. Asay, L. P. Mix, and F. C. Perry. Ejection of material from shocked surfaces. *Applied Physics Letters*, 29:284–287, 1976.

[17] P. Andriot, P. Chapron, and F. Olive. Ejection of material from shocked surfaces of tin, tantalum and lead-alloys. *AIP Conference Proceedings*, 78:505–509, 1982.

[18] R Couch, L Shaw, R Barlett, L Steinmetz, W Behrendt, and C Firpo. SURFACE PROPERTIES OF SHOCKED LEAD. *J. Phys. Colloques*, 46(C5):385–393, 1985.

[19] Roger Cheret, Pierre Chapron, and Philippe Elias. Mass ejection from the free surface of shock-loaded metallic samples. In *In: Gumpta Y.M. (eds) Shock Waves in Condensed Matter.*, pages 651–654. Springer, Boston, MA, Boston, MA, 1986.

[20] W. S. Vogan, W. W. Anderson, M. Grover, J. E. Hammerberg, N. S.P. King, S. K. Lamoreaux, G. MacRum, K. B. Morley, P. A. Rigg, G. D. Stevens, W. D. Turley, L. R. Veeser, and W. T. Buttler. Piezoelectric characterization of ejecta from shocked tin surfaces. *Journal of Applied Physics*, 98(113508), 2005.

[21] M. B. Zellner, M. Grover, J. E. Hammerberg, R. S. Hixson, A. J. Iverson, G. S. MacRum, K. B. Morley, A. W. Obst, R. T. Olson, J. R. Payton, P. A. Rigg, N. Routley, G. D. Stevens, W. D. Turley, L. Veeser, and W. T. Buttler. Effects of shock-breakout pressure on ejection of micron-scale material from shocked tin surfaces. *Journal of Applied Physics*, 102(013522), 2007.

[22] M. B. Zellner, W. Vogan McNeil, J. E. Hammerberg, R. S. Hixson, A. W. Obst, R. T. Olson, J. R. Payton, P. A. Rigg, N. Routley, G. D. Stevens, W. D. Turley, L. Veeser, and W. T. Buttler. Probing the underlying physics of ejecta production from shocked Sn samples. *Journal of Applied Physics*, 103(123502), 2008.

[23] Michael B. Zellner, Guy Dimonte, Timothy C. Germann, James E. Hammerberg, Paulo A. Rigg, Gerald D. Stevens, William D. Turley, and William T. Buttler. Influence of shockwave profile on ejecta. *AIP Conference Proceedings*, 1195:1047–1050, 2009.

[24] Yongtao Chen, Haibo Hu, Tiegang Tang, Guowu Ren, Qingzhong Li, Rongbo Wang, and William T. Buttler. Experimental study of ejecta from shock melted lead. *Journal of Applied Physics*, 111(053509), 2012.

[25] S. K. Monfared, D. M. Oró, M. Grover, J. E. Hammerberg, B. M. Lalone, C. L. Pack, M. M. Schauer, G. D. Stevens, J. B. Stone, W. D. Turley, and W. T. Buttler. Experimental observations on the links between surface perturbation parameters and shock-induced mass ejection. *Journal of Applied Physics*, 116(063504), 2014.

[26] D. S. Sorenson, R. W. Minich, J. L. Romero, T. W. Tunnell, and R. M. Malone. Ejecta particle size distributions for shock loaded Sn and Al metals. *Journal of Applied Physics*, 92:5830–5836, 2002.

[27] V. A. Ogorodnikov, A. L. Mikhaĭlov, V. V. Burtsev, S. A. Lobastov, S. V. Erunov, A. V. Romanov, A. V. Rudnev, E. V. Kulakov, Yu B. Bazarov, V. V. Glushikhin, I. A. Kalashnik, V. A. Tsyganov, and B. I. Tkachenko. Detecting the ejection of particles from the free surface of a shock-loaded sample. *Journal of Experimental and Theoretical Physics*, 109(3):530–535, 2009.

[28] S. K. Monfared, W. T. Buttler, D. K. Frayer, M. Grover, B. M. Lalone, G. D. Stevens, J. B. Stone, W. D. Turley, and M. M. Schauer. Ejected particle size measurement using Mie scattering in high explosive driven shockwave experiments. *Journal of Applied Physics*, 117(223105), 2015.

[29] D. R. Guildenbecher, C. López-Rivera, and P. E. Sojka. Secondary atomization. *Experiments in Fluids*, 46:371–402, 2009.

[30] W. T. Buttler, S. K. Lamoreaux, R. K. Schulze, J. D. Schwarzkopf, J. C. Cooley, M. Grover, J. E. Hammerberg, B. M. La Lone, A. Llobet, R. Manzanares, J. I. Martinez, D. W. Schmidt, D. G. Sheppard, G. D. Stevens, W. D. Turley, and L. R. Veeser. Ejecta Transport, Breakup and Conversion. *Journal of Dynamic Behavior of Materials*, 3(2):334–345, 2017.

[31] William T. Buttler. (U) Ejecta transport breakup and conversion : DR Progress report. Technical report, LA-UR-19-21158, 2019.

[32] Stephen R. Turns. *An introduction to combustion : concepts and applications.* McGraw-Hill, New York, 2nd edition, 2006.

[33] Thierry Poinsot and Denis Veynante. *Theoretical and Numerical Combustion.* R. T. Edwards, Philadelphia, 2nd edition, 2005.

[34] Irvin Glassman. *Combustion.* Academic Press, San Diego, CA, 3rd edition, 1996.

[35] J D Schwarzkopf, D G Sheppard, J E Hammerberg, M M Schauer, W T Buttler, and R K Schulze. Modeling of Ce ejecta in He (non-reactive) and D2 (reactive) gases. In *21st Biennial Conference of the APS Topical Group on Shock Compression of Condensed Matter (SHOCK2019)*, Portland, OR, 2019.

[36] William L. Korst and James C. Warf. Rare Earth-Hydrogen Systems. I. Structural and Thermodynamic Properties. *Inorganic Chemistry*, 5(10):1719–1726, 1966.

[37] W E Ranz and W R Marshall. Evaporation from Drops. *Chemical Engineering Progress*, 48(3):141–146, 1952.

[38] C T Crowe, J D Schwarzkopf, M Sommerfeld, and Y Tsuji. *Multiphase Flows with Droplets and Particles.* CRC Press, 2 edition, 2012.

[39] Cerium - Ce, https://www.lenntech.com/periodic/elements/ce.htm, 2019.

[40] Deuterium - Gas Encyclopdeia, https://encyclopedia.airliquide.com/deuterium, 2019.

[41] A. S. Chernikov, V. I. Savin, V. N. Fadeev, N. A. Landin, and L. A. Izhvanov. Thermodynamic and physical properties of yttrium and some rare earth hydrides. *Journal of The Less-Common Metals*, 130:441–452, 1987.